Deep neural network classification of in vivo burn injuries with different etiologies using terahertz time-domain spectral imaging

OMAR B. OSMAN,[1] ZACHERY B. HARRIS,[1] MAHMOUD E. KHANI,[1] JUIN W. ZHOU,[1] ANDREW CHEN,[1] ADAM J. SINGER,[2] AND M. HASSAN ARBAB[1,*]

[1]*State University of New York at Stony Brook, THz Biophotonics Laboratory, Department of Biomedical Engineering, 101 Nicolls Rd., Stony Brook, NY 11794, USA*
[2]*Renaissance School of Medicine at Stony Brook University, Department of Emergency Medicine, 101 Nicolls Rd., Stony Brook, NY 11794, USA*
*hassan.arbab@stonybrook.edu

Abstract: Thermal injuries can occur due to direct exposure to hot objects or liquids, flames, electricity, solar energy and several other sources. If the resulting injury is a deep partial thickness burn, the accuracy of a physician's clinical assessment is as low as 50-76% in determining the healing outcome. In this study, we show that the Terahertz Portable Handheld Spectral Reflection (THz-PHASR) Scanner combined with a deep neural network classification algorithm can accurately differentiate between partial-, deep partial-, and full-thickness burns 1-hour post injury, regardless of the etiology, scanner geometry, or THz spectroscopy sampling method (ROC-AUC = 91%, 88%, and 86%, respectively). The neural network diagnostic method simplifies the classification process by directly using the pre-processed THz spectra and removing the need for any hyperspectral feature extraction. Our results show that deep learning methods based on THz time-domain spectroscopy (THz-TDS) measurements can be used to guide clinical treatment plans based on objective and accurate classification of burn injuries.

1. Introduction

Burn injuries are primarily caused by exposure to hot objects, hot liquids, direct flames, solar energy, electricity or corrosive chemicals [1]. More specifically, the majority of burn injuries in children under the age of five are caused by exposure to a hot object or scalding liquid [1]. The prognosis of a burn patient depends on the depth of dermal injury and total body surface area affected by the burn. If the burn only affects the epidermal layer, the tissue will reepithelialize spontaneously. Superficial partial-thickness burns injure both the epidermis and the dermal layers of the skin and still can spontaneously heal via reepithelialization. On the other hand, deep partial-thickness burns can progress into full-thickness state and require surgical excision and grafting. Deep partial-thickness burns are challenging to diagnose because it can take several days before a physician can determine whether or not burn wound progression has occurred. Clinical assessment of deep-partial thickness or indeterminate burns has been shown to have an accuracy as low as 50-76% [2–4], which is likely attributed to the poorly understood complexity of the wound conversion process [5]. Furthermore, early excision and grafting results in shorter hospital stays, lower cost of care, and overall better patient outcomes [2,6,7]. Therefore, early prediction of wound conversion outcomes, assisted by a diagnostic technology, would greatly improve patient care [8].

While the first step in the standard-of-care for burn management is a qualitative visual and tactile clinical assessment of the injuries, there have been several technologies that propose methods for early quantitative assessment of these wounds. Typically, these techniques use light

waves, sound waves or a combination of the two [9]. Laser Doppler imaging (LDI), which is one of the most well-studied modalities for burn wound diagnosis, has been tested clinically [10] and is approved by the FDA [11]. In classifying burns that heal within 21 days, LDI has a 95% accuracy when imaging is performed 3 days post-burn and between 54% and 79.5% accuracy when imaging on earlier days [12]. Other promising techniques for burn diagnosis include photoacoustic imaging [13,14], polarization-sensitive optical coherence tomography [15], and thermal imaging [16], to name a few. In recent years, spatial frequency-domain imaging has emerged as a new burn diagnosis modality. It has been shown to accurately diagnose burn depth in an animal model [17] and improve diagnostic accuracy in a clinical setting [18]. Additionally, multi-spectral imaging has demonstrated the ability to classify burn depth and assist physicians in determining the proper depth of wound debridement [19]. While many of these modalities have been tested in clinical and pre-clinical settings, none have reached clinical adoption. Unlike these techniques, the signal contrast in THz-TDS imaging is based on the skin tissue hydration and electromagnetic scattering from viable skin appendages [20], which play a major role in the wound healing process [21].

The inception of the idea for using THz-TDS for imaging the extent of burn injuries emerged when Mittleman et al. observed a strong signal contrast in the terahertz (THz) spectra between raw and burned chicken muscle flesh [22]. Since this preliminary report, THz-TDS has shown great promise for imaging burn injuries in preclinical models that are more relevant to human skin. Studies using ex-vivo porcine skin [23] and in-vivo rats [24] showed that the primary contrast mechanism in THz assessment of burn injuries was a difference in the tissue water content between burned and healthy skin. More recent work has shown a strong correlation with MRI in a burn induced model of edema [25]. Moreover, image processing techniques have been proposed for co-registration between THz and visual images of burns [26]. Furthermore, typical wound ointments and bandages have a relatively low absorption coefficient at THz wavelengths [27], suggesting an additional potential benefit when imaging through wound dressings. In addition to characterization of skin burns, THz modalities have recently been used for delineation of breast carcinoma [28], corneal hydration mapping [29–31], microscopic assessment of biomolecular structure [32], visualizing skin moisturizer effects [33], monitoring drug delivery of transdermal patches [34], skin hydration assessment [35–37], characterizing tissue-equivalent samples [38], detection of blood cancer [39], and several others [40]. Machine learning techniques applied to THz biomedical imaging have also been shown to produce high accuracy methods to classify invasive ductal carcinoma [41,42] and basal cell carcinoma [43], assess traumatic brain injury [44], and diagnose cervical carcinoma [45]. While numerous machine learning algorithms exist for THz biomedical applications, the specific methodology should be selected based on the properties and constraints of the THz spectral data set. A thorough comparison of machine learning approaches for THz biomedical applications can be found in [46].

Our previous work in diagnosis of burn injuries has suggested that the tissue hydration may not be the only contrast mechanism for differentiating burns using the THz-TDS modality. Combining the THz amplitude with the spectral roll-off (computed as the spectral slope) of in vivo burn injuries in rats suggests that additional signal contrast parameters, such as electromagnetic scattering, can help improve the characterization of burn injuries [20,47,48]. Further, using a commercial point-spectroscopy THz-TDS system, we showed that this hyperspectral parameter could be used to differentiate in vivo porcine burns with varying depths immediately after burn induction [49]. While these early THz spectroscopic studies were a major milestone in burn assessment applications, imaging large animals or humans is impractical with a point-spectroscopy system because the subject would need to be raster scanned.

To mitigate the challenge of in vivo THz studies, several groups have developed handheld point spectroscopy [50] and line scanning [51] measurement systems. More recently, we developed a handheld 2-dimensional THz-TDS imaging system for in vivo and clinical applications [52].

We used this THz-PHASR Scanner and the hyperspectral Z parameter to show that broadband THz measurements can differentiate between shallow and deep partial-thickness burns, as well as monitor their wound healing progression over a period of 5 days after injury [53].

In this study, we present the application of the THz-PHASR Scanner and a neural network classification algorithm in a porcine burn model to evaluate the classification accuracy of assessing burn injuries in vivo. Previous work has shown that THz-TDS imaging can differentiate burns when the study was carried out with a single etiology [49,53]. However, in a clinical setting, the etiology of thermal injuries come from various sources. Some researchers have even suggested a difference in pathophysiology when comparing scald and contact burns [54,55]. To address this question, our animal model contained both scald and contact burn injuries of similar conditions. Further, our results here contain an additional source of variability by utilizing two versions of the THz-PHASR Scanner and two THz-TDS sampling techniques: Asynchronous OPtical Sampling (ASOPS) [56] and Electronically Controlled OPtical Sampling (ECOPS) [57]. The second version of the THz-PHASR Scanner, reported elsewhere [58], enjoys a larger field-of-view and a 20-fold increase in the scan speed per pixel using the ECOPS technique. Our results show that the THz-PHASR Scanner with a deep neural network algorithm can accurately classify partial-, deep partial-, and full-thickness burns, independent of scanning hardware, the time-domain sampling methodology, or contact and scald etiology (Receiver Operating Characteristic- Area Under the Curve (ROC-AUC) = 91%, 88%, and 86%, respectively).

2. Materials and methods

2.1. Animal protocol and burn induction

The experimental protocol used in this study was reviewed and approved by the Institutional Animal Care and Use Committee at the Stony Brook University. This study included three female Landrace pigs weighing approximately 30-50 kg (12-16 weeks). On the day of burn induction, the animals were sedated with an intramuscular injection that consisted of ketamine (20 mg/kg), xylazine (2.2 mg/kg), acepromazine (0.1 mg/kg), and atropine (0.02 mg/kg), and then anesthetized with a continuous flow of 0.5–5% isoflurane via an endotracheal tube. To prepare the pig for burn induction, we washed the skin with soap and water, trimmed and shaved the hair, and used a stencil to mark the locations of the burns. Immediately following burn induction, the veterinary staff administered an intramuscular injection of buprenorphine (0.005-0.02 mg/kg) and placed a transdermal fentanyl patch (50 μg/kg) proximal to the tail. Additionally, each burn was gently scraped with the blunt end of sterilized forceps to remove the necrotic epidermal layer, consistent with standard debridement in clinical management of burns.

During THz imaging experiments, each pig was kept on isoflurane and monitored by the veterinary staff of the Division of Laboratory Animal Research at Stony Brook University. After imaging, we treated each burn by applying triple antibiotic ointment (Bacitracin Zinc, Neomycin Sulfate, Polymyxin B Sulfate; Taro Pharmaceuticals, Hawthorne, New York) and covered the wound with non-adherent Telfa pads (Medline Industries Inc, Northfield, IL, USA) and transparent Tegaderm sheet (3M, Saint Paul, MN, USA). After dressing the wounds, we wrapped the midsection of the pig with flexible gauze bandage and Tensoplast adhesive bandage (BSN Medical, Hamburg, Germany). Punch biopsies with diameters between 4 and 8 mm were collected on the day of burn induction (Day 0).

Each pig received 20 burns on their dorsal side with systematically distributed etiologies (metallic contact vs hot water scald) and varying severities to account and control for anatomical variations [49]. These example etiologies were chosen because they are clinically representative of many real-world burn injuries [1]. Furthermore, scald burns should provide relatively high inter-group homogeneity [59,60] and contact burns are well validated in the literature for large [61] and small burn injuries [62–64]. As shown in Fig. 1(a), the first method of burn induction was with a contact device, which was created using a square brass bar and a spring loaded tube to

maintain constant pressure (2 kg / 6.25 cm^2). The contact device maintained a steady temperature with an internal heating element and thermocouple. This device has the capability of maintaining temperatures up to 160°C. As shown in Fig. 1(b), the second method of burn induction was using a standardized hot water scald device [60]. This device consisted of a stainless steel pipe with a hot water inlet and a vacuum outlet (Adafruit Industries, New York, NY, USA) to constantly cycle hot water through the device and onto the surface of the skin. The foam on the bottom of the pipe was folded over to create a watertight seal. Water temperature was controlled with an immersion circulation heater (Haake, Thermo Fisher Scientific, Waltham, MA, USA). Hot water would flow from the immersion heater through high-temperature rubber tubing and would lose approximately 2-3°C before reaching skin. The illustrated cross-sections of each device are shown in Fig. 1(c-d).
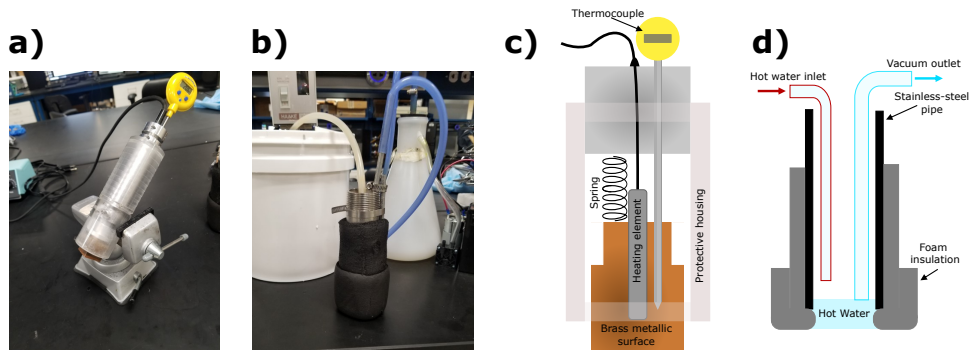

Fig. 1. The brass contact and scalding devices used to induce controlled degrees of burn injuries are shown as visual images (a,b) and illustrated cross-sections (c,d), respectively.

The burn severity conditions described in Table 1 show the 14 different burn conditions included in this study, where either the temperature was kept constant and the exposure time was varied (between 5-60 seconds) or the time was constant and temperature was varied between 70°C and 98°C. In addition to the burn conditions, we imaged 9 healthy unburned areas as control experiments. All tissue sites were approximately 4 cm apart from each other. Moreover, in two of the pigs, we created similar mixtures of severity conditions between contact and scald etiologies, whereas the third pig contained only scald burns. Severity conditions were chosen based on literature and previous animal models to provide a distribution of burns ranging from superficial to full thickness injuries [65].

2.2. Histological assessment

Sections from biopsies were stained with Hematoxylin & Eosin (H&E) and assessed for damage on Day 0. Fig. 2(a-b) shows an example of a superficial partial-thickness burn (18% of dermal depth) and Fig. 2(c-d) presents a deeper partial-thickness burn injury (80% of dermal depth). We utilized a standardized approach to evaluate the depth of damage, where signs of dermal injury included vascular damage or blockage, collagen damage, and dermal appendage damage [66]. Burn depth was determined by locating the depth of the deepest point of dermal injury normalized by the total dermal thickness. The black arrows in Fig. 2(b) and 2(d), which represent the 20× magnification of the black boxes drawn in Fig. 2(a) and 2(c) respectively, show typical examples of vascular blockage. Also, the yellow arrow in Fig. 2(d) shows an example of dermal appendage damage.

Table 1. Describes the number, temperature, duration and type for each burn severity condition across three animals.

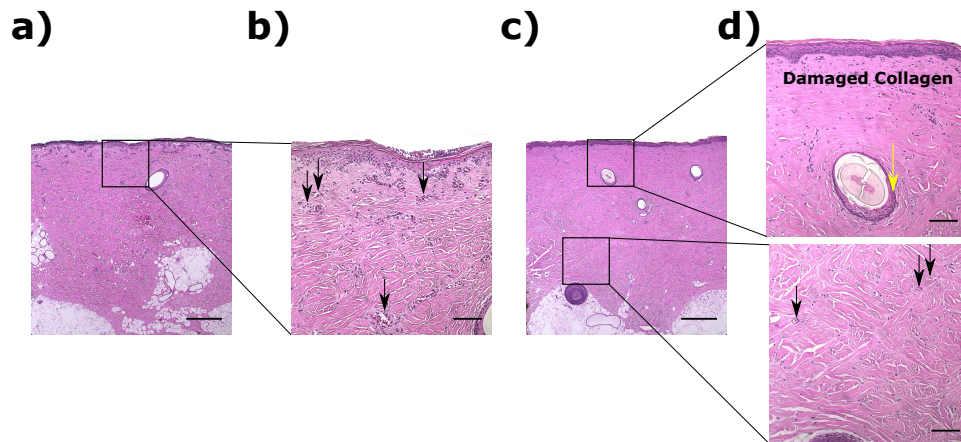| N	Duration (s)	Temperature (°C)	Type
9	0	N/A	Healthy
9	5	98	Scald
4	5	98	Contact
4	10	70	Scald
3	10	80	Scald
4	10	70	Contact
3	10	80	Contact
1	10	90	Contact
6	10	98	Scald
5	10	98	Contact
3	15	98	Scald
3	15	98	Contact
5	25	98	Scald
5	45	98	Scald
5	60	98	Scald

Fig. 2. (a) shows an example of a superficial partial-thickness burn at 5× magnification and (b) 20× magnification (zoomed in the black box drawn in (a)). A deeper partial-thickness burn is shown at 5× magnification in (c) and a 20× magnification (d) over the black box insets in (c). Black arrows point to vascular blockage and the yellow arrow point to a dermal appendage damage. Scale bars are 500 μm in (a) and (c) and 100 μm in (b) and (d).

2.3. Terahertz handheld scanner

THz imaging of the burn injuries was performed using multiple versions of our THz-PHASR Scanner [52,67]. Fig. 3(a-c) show renderings of the 3D printed housing of the PHASR Scanner iteration associated with each of the animal studies. Fig. 3(d) shows the generalized optical schematic describing the layout design of all PHASR Scanners. Briefly, the emitted THz beam passes through a Si beamsplitter and is reflected from a gimballed mirror mounted on a motorized scanning mount. The scanning motors steer THz radiation by pivoting the beam at the real

focal point of a custom-fabricated telecentric f-θ lens made from high density polyethylene to maintain focus across a flat imaging plane [67–69]. The focused THz beam passes through a fused silica imaging window, reflects from the surface of the sample and is directed through the same optics back towards the detector. THz radiation was generated and detected using a commercially available fiber-coupled photoconductive antenna (PCA) pair as part of a THz-TDS system (Menlo Systems Inc, Newton, NJ, USA). This system uses one femtosecond laser to pump an InGaAs/InAlAs PCA emitter and a second femtosecond laser to probe an LT InGaAs/InAlAs PCA antenna detector.
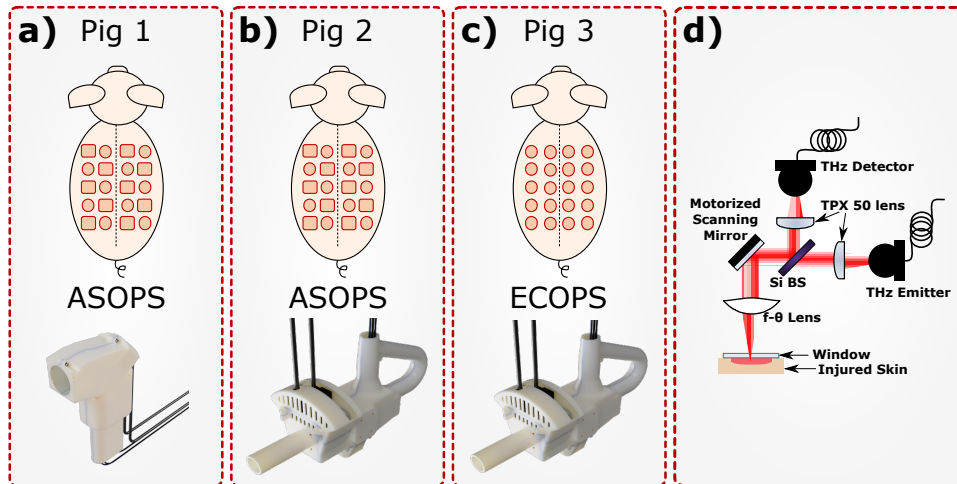

Fig. 3. The three animal subjects are depicted along with 3D renderings of the corresponding version of the THz-PHASR Scanner used in each arm of the study. (a) illustrates Pig 1 where we used a porcine scald (circles) and contact (squares) burn model with PHASR 1.0 and an ASOPS THz-TDS system. (b) illustrates Pig 2 where we used a porcine scald and contact model with PHASR 2.0 and an ASOPS THz-TDS system. (c) illustrates Pig 3 where we used a porcine scald model with PHASR 2.0 and an ECOPS THz-TDS sampling method using the same ASOPS hardware. In these illustrations, red squares represent contact burns and red circles represent scald burns. (d) illustrates the general optical schematic used in all iterations of the PHASR Scanner.

In this study, we used three versions of the THz-PHASR Scanner. The first device, PHASR 1.0, is described in Fig. 3(a) and used a mirror mounted in a miniature motorized gimbal (T-OMG, Zaber Technologies Inc, Vancouver, BC, CA) to telecentrically steer the beam across a custom-made f-θ lens. Using PHASR 1.0, our THz images were limited to a 12×19 mm^2 field-of-view (FOV) because of the limited angular travel range of the two motors and intercoupling of the scanning axes of the gimbal mount [68]. The second iteration, PHASR 2.0, is described in Fig. 3(b). Here, we improved the FOV by implementing a heliostat-based gimbal design using a goniometer (GSM, Zaber Technologies Inc, Vancouver, BC, CA) and a rotation stage (RSM, Zaber Technologies Inc, Vancouver, BC, CA). The new design in PHASR 2.0, resulted in an increased FOV of 27×27 mm^2. While the scanning hardware had the capability of an even larger FOV, we opted for a smaller scan range due to the limitations of the ASOPS time-domain sampling acquisition rate. The final iteration of the PHASR device, described in Fig. 3(c), included the same hardware as in PHASR 2.0, but improved the data acquisition time over 20-fold by adapting the existing TERA ASOPS hardware to use an ECOPS method to acquire the THz-TDS signal at each pixel [57,58,70]. More details about the implementation and comparison of the ASOPS and ECOPS sampling methods can be found in [57,58,70].

2.4. Signal processing

Fig. 4 describes the signal processing flow chart used in this study for pre-processing and training of the deep neural network. The data collected by the THz-PHASR Scanner is organized in the form of 2D images consisting of a full THz-TDS signal in each pixel. We also acquired a reference THz-TDS image by scanning a fused silica imaging window without a sample present. A bandpass filter was applied to the raw time-domain (TD) signal to remove noise outside of the usable THz bandwidth. Once filtered, the TD signals were denoised with a wavelet-based hard thresholding algorithm [71,72]. After filtering and denoising, the TD signals were Fourier Transformed and deconvolved by the reference measurement using the Wiener deconvolution algorithm [73] to minimize the effect of residual noise where the SNR is poor.
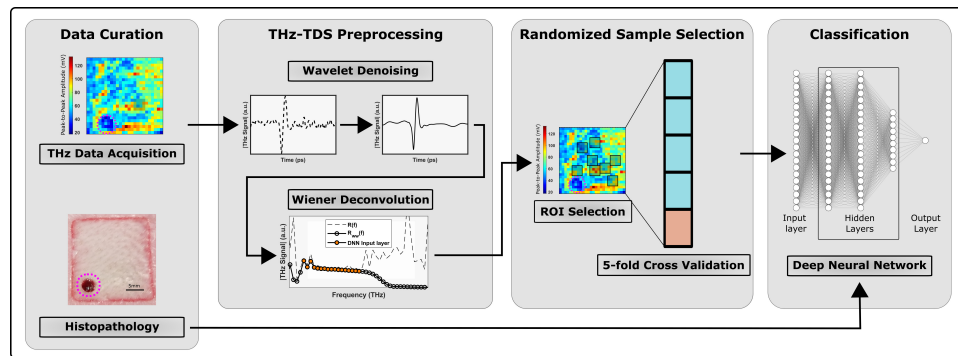

Fig. 4. The signal processing flowchart. After burn creation, THz-TDS images were acquired from each burn. The THz-TDS signals of each pixel were bandpass filtered and denoised with a wavelet hard-thresholding algorithm. Time domain sample signals were Fourier transformed and deconvolved by a fused silica reference using a Wiener deconvolution algorithm. Up to 8 random ROIs were selected on each burn and the mean preprocessed spectra of each ROI was used as the input layer to the neural network. Burn depth, determined by histopathology, was used as the ground truth for the neural network classification.

2.5. Neural network and ROI selection

Up to 8 4×4 ROIs (consisting of 16 pixels each) were randomly selected in each THz burn image. The wavelet-denoised and Wiener deconvolved THz spectral amplitude, $R_{ww}(f)$, was averaged over the pixels in each ROI and used as an input into our neural network (NN) classification algorithm. Averaging sample measurements from within the ROI allowed us to mitigate some of the detrimental effects of electromagnetic scattering [74]. Further, we excluded pixels from the ROI selection process that clearly showed poor contact between the skin and imaging window. Poor contact was determined by examining the TD signal for multiple Fabry-Perot reflections by a window-air gap interface.

Illustrated in the "Classification" block in Fig. 4, we employed a fully connected sequential neural network using the Keras deep learning framework in Python. Our model takes $R_{ww}(f)$, between 0.17 THz to 0.56 THz as the input layer and outputs a single classification prediction. The input layer for all samples was normalized using a standard scaler from Sci-kit Learn. The model contained 3 hidden layers, where the first two layers consisted of 20 nodes each and the third layer contained 10 nodes. Each layer was initialized with a Glorot normal initializer [75] and used an exponential linear unit activation function. To optimize the model, we used Stochastic Gradient Descent and the binary cross-entropy loss function. Hyperparameters in the neural network were chosen by a grid search to maximize accuracy. The algorithm was run for 2000

epochs with a learning rate of 0.005 and took approximately 3.4 minutes to complete training and testing for 5-fold cross-validations using a single processor core. We also investigated a squared-hinge loss function and various activation functions but found no improvement in the accuracy of the classifier.

3. Results

Fig. 5 illustrates our signal processing method for representative partial thickness, deep partial-thickness, and full-thickness burns with thermal damage reaching 18%, 90%, and 107% of the dermis thickness, respectively. Fig. 5(a-c) shows the visual images of the burns, where partial-thickness burns can be easily distinguished from the deep partial- and full-thickness burns. On the other hand, the deep partial- and full-thickness burns could not be differentiated from each other solely based on the visual images in Fig. 5(b-c). The peak-to-peak amplitude THz images in Fig. 5(d-f) show that, while some burns have slightly higher reflectivity in certain areas, they are practically indistinguishable. Fig. 5(g-i) show the mean deconvolved THz signal over a single ROI, where the blue trace and filled area represent the mean and standard deviation of the denoised signal, $R_{ww}(f)$. The red area in Fig. 5(g-i) represents the standard deviation of the signal prior to the wavelet-based denoising algorithm and Wiener deconvolution, $R(f)$. By comparing the red and blue areas in Fig. 5(g-i), it is clear that wavelet denoising and Wiener deconvolution offer a strong improvement in the signal to noise. The improvement is especially pronounced in areas where the SNR is low, such as near the upper and lower limits of our usable bandwidth. Comparing the THz spectra of a representative partial thickness burn in Fig. 5(g) and representative deep partial- or full-thickness burn in Fig. 5(h-i) shows a decrease in the THz amplitude after 0.5 THz. This phenomenon is consistent with prior work in rodent models, where the density of viable skin structures provided an additional THz signal contrast mechanism for deep and shallow burns [20]. The effect of scattering by such skin structures is dependent on several factors, such as wavelength, particle size, dielectric contrast variations, density [76,77], and roughness [78]. These variables can be experimentally observed by the aggregate effect of electromagnetic scattering as a frequency-dependent loss in energy reflected in the specular direction, or otherwise by the increased reflectivity in the off-specular angles. However, teasing out diagnostic information regarding the viability and intactness of skin structures that are critical in the skin regeneration processes using THz-TDS measurements, is complex and would require extensive instrumentation, experimentation and modeling. Since our ultimate goal in this study is classification of burn injuries, deep neural networks and machine learning algorithms are ideal non-linear tools for extracting these effects and using the signal contrast for classifying burns based on their THz spectra.

To classify the burn injuries, we defined full-thickness burns as any injury showing damage greater than or equal to 100% of total thickness of the dermis. Deep-partial thickness burns were defined as injuries containing damage in the deepest third of the dermis: greater than or equal to 67% and less than 100% of the dermal thickness. Finally, partial thickness burns were defined as injuries containing damage in the first two thirds of the dermis: less than 66% of the dermal thickness. We assessed the classification accuracy of our neural network using a "one vs. all" testing approach for each class of burns. All classifications were run using 5-fold cross-validation, where the entire dataset was randomly split into 80% training data and 20% testing data. The cross-validation process was repeated 5 times to ensure that all data had an opportunity to appear in the testing set and the mean performance metrics were reported in Fig. 6 and Table 2. Because the ROI selection process was random, we repeated the ROI selection and classification process 10 times to avoid bias due to the randomized location within the burns. Performance metrics in Fig. 6 and Table 2 were averaged for all 10 randomized ROI sampling iterations. Fig. 6(a) shows the receiver operator characteristics (ROC) curve for the classification of partial thickness burns with ROC-AUC of 0.91. In deep partial-thickness burns, Fig. 6(b) shows that we observed
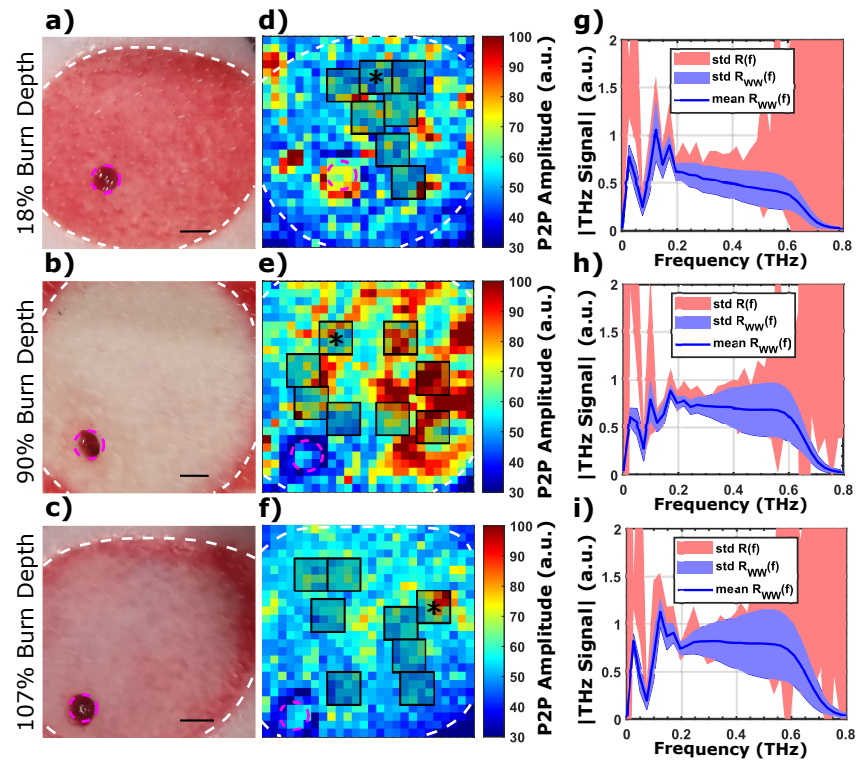
Fig. 5. Visual (a-c) and THz images (d-f) of representative partial-thickness, deep partial-thickness burns, and full-thickness burns, having a burn depth of 18%, 90% and 107%, respectively. (d-f) show examples of the randomized ROI selection (black rectangles), and their respective example THz spectra (g-i) from a single representative ROI (marked by the asterisks). The white dashed lines in (a-f) depict the wound margin and the magenta circles show the locations of the corresponding biopsies. The color axis represents peak-to-peak (P2P) amplitude of the THz-TDS signal. The size of each pixel was 1×1 mm^2. The blue trace and area in (g-i) represent the mean and standard deviation of $R_{ww}(f)$, and the red area represents the standard deviation of R(f). The mean and standard deviation were calculated using all pixels in a corresponding 4×4 pixel ROI . The scale bar in (a-c) represents 5 mm.

slightly lower classification capability (ROC-AUC of 0.88) compared to partial thickness burns. Full thickness burns were classified with an ROC-AUC of 0.86. In addition to the ROC-AUC metric, we have tabulated the classification accuracy, specificity, and sensitivity in Table 2.

Table 2. Describes the ROC-AUC, accuracy, sensitivity and specificity for partial-thickness deep partial-thickness, full-thickness burn groups.

	Partial-Thickness	Deep Partial-Thickness	Full-Thickness
ROC-AUC	91.00%	87.60%	86.30%
Accuracy	86.80%	80.30%	83.30%
Sensitivity	58.30%	73.30%	59.70%
Specificity	93.10%	85.50%	91.20%

We found that partial-thickness burns could be classified more accurately than deep partial- and full thickness burns. This phenomenon is likely attributed to the penetration depth of the
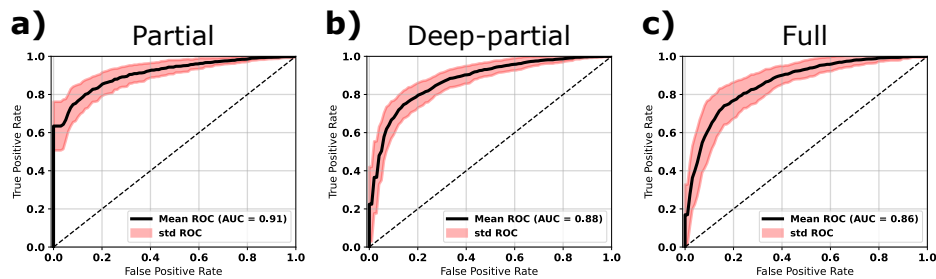
Fig. 6. The resulting ROC curves are shown for partial-thickness (a), deep partial thickness (b), and full thickness (c) burns, with a resulting ROC-AUC of 0.91, 0.88, and 0.86, respectively. The black trace and red area represent the mean and standard deviation of ROC curves after 5-fold cross validation and 10 repeated samplings of randomized ROIs.

THz signal, which is between 0.1 mm and < 1 mm in healthy human skin [79]. Furthermore, in most thermal injuries, heat is exposed at the outermost layer of the skin and propagates axially (towards the subcutaneous tissue) and laterally (towards the surrounding tissue). As a result, the most superficial areas of the injury will experience the most thermal damage. Because we expect to observe more spectral change in burns with increasing thermal damage, the THz spectra from the more superficial areas of the burn should serve as a proxy for the overall burn depth. This effect explains the observed high classification performance in deep partial- and full-thickness burns even though the THz signal cannot penetrate to the deepest parts of the skin. Future studies using higher power THz sources with an increased penetration depth would likely improve classification accuracy for deeper burns. In addition to classification of the burn injuries, our algorithm classified the healthy unburned controls with ROC-AUC = 95% and accuracy = 93%.

4. Discussion

Most previous preclinical reports that used the THz spectra to characterize burns were carried out with a burn induction protocol using a single etiology [24,49,53]. However, in a clinical setting, the source of burn injuries typically vary between a multitude of sources, such as scald, contact, flame, and steam. Our study blinds the user to the etiology of injury and shows that the THz-PHASR Scanner can accurately classify partial-, deep partial-, and full-thickness burns based on the histological assessment of the depth of injury.

The results presented here provide the foundational methodology for future work in clinical trials. The handheld component of the THz-PHASR Scanner is connected to the laser and electronic systems by an umbilical attachment. This system can be easily deployed to the patient rooms without any additional modifications. However, while the preprocessing methodology and the neural network algorithm show high classification accuracy in the animal studies, new training data sets with final clinical outcomes will be required for accurate burn diagnosis in human subjects.

Swines are a clinically accepted model for burn injuries. We chose a porcine model over rodent models of burn injuries because of anatomical and physiological similarity to human skin [59]. In addition, the genomic and proteomic responses to inflammatory diseases (i.e. burn injuries and sepsis) of swines resemble that of humans more closely than rodents [80]. By choosing a porcine model over a rodent model, we inherently limit our ability to use a large sample size. However, we systematically distributed 20 burns on each pig to account for within subject variations.

Our prior work in differentiating burns using THz reflection spectra was based on a hyperspectral parameter, called the Z-metric [49,53]. The Z-metric is a linear combination of the upper and lower bounds of frequency dependent spectral slopes and the normalized deconvolved spectral

amplitude within a -10 dB bandwidth. Here, we simplified the classification process by leveraging supervised deep learning techniques. The pre-processed and Wiener deconvolved THz spectra were directly used as the input layer to our deep neural network. Compared to the Z-metric method, this approach reduces the number of pre-processing steps required to create a robust classification method for partial-thickness burn injuries.

Supervised machine learning algorithms, such as deep neural networks, typically require large datasets for high quality classification. While our study contained a total of 60 burns from three animals, each burn contains heterogeneity from multiple aspects: within each burn [49], anatomical variations, severity between burn grades and between animal subjects. The THz-PHASR Scanner enabled resolving this heterogeneity and utilizing it in our classification algorithm. Additionally, we achieved high accuracy after combining the THz-TDS data from three different implementations of the PHASR Scanner, two burn induction models (contact vs scald), and several severity conditions. This scale of variations emphasizes that our pre-processing and deep neural network classification methods are robust techniques, which can be used in similar THz biophotonics and biosensing studies.

5. Conclusion

In conclusion, we present the application of the THz-PHASR Scanner and a deep neural network algorithm to classify burn injuries in vivo. Burn centers will typically receive patients with many different burn etiologies [1]. Researchers also have suggested differences in the pathophysiology of contact and scald burns [54,55]. By including multiple etiologies, multiple scanning geometries and multiple THz-TDS sampling methods, we have shown that our robust method for characterizing burn injuries gives an AUC-ROC of 91%, 88%, and 86% for classifying partial-, deep partial-, and full-thickness burns, respectively. The techniques reported in this paper, in turn, can provide burn physicians with additional information about the depth of burn injuries to improve patient care.

Disclosures. P: MHA discloses intellectual property owned by the University of Washington, US Patent No. US9295402B1 [81].

Data availability. Data presented in this paper are not publicly available at this time but may be obtained from the authors upon request.

References

1. M. D. Peck, "Epidemiology of burns throughout the world. part i: Distribution and risk factors," Burns **37**(7), 1087–1100 (2011).
2. D. M. Heimbach, M. A. Afromowitz, L. H. Engrav, J. A. Marvin, and B. Perry, "Burn depth estimation–man or machine," The J. Trauma **24**(5), 373–378 (1984).
3. P. Hlava, J. Moserova, and R. Königová, "Validity of clinical assessment of the depth of a thermal injury," Acta Chir. Plast. **25**(4), 202–208 (1983).
4. B. S. Atiyeh, S. W. Gunn, and S. N. Hayek, "State of the art in burn treatment," World J. Surg. **29**(2), 131–148 (2005).
5. V. Singh, L. Devgan, S. Bhat, and S. M. Milner, "The pathogenesis of burn wound conversion," Annals of plastic surgery **59**(1), 109–115 (2007).
6. Y. S. Ong, M. Samuel, and C. Song, "Meta-analysis of early excision of burns," Burns **32**(2), 145–150 (2006).
7. D. T. Gray, R. W. Pine, T. J. Harnar, J. A. Marvin, L. H. Engrav, and D. M. Heimbach, "Early surgical excision versus conventional therapy in patients with 20 to 40 percent burns: a comparative study," The Am. J. Surg. **144**(1), 76–80 (1982).
8. M. P. Rowan, L. C. Cancio, E. A. Elster, D. M. Burmeister, L. F. Rose, S. Natesan, R. K. Chan, R. J. Christy, and K. K. Chung, "Burn wound healing and treatment: review and advancements," Critical care **19**(1), 243 (2015).
9. J. E. Thatcher, J. J. Squiers, S. C. Kanick, D. R. King, Y. Lu, Y. Wang, R. Mohan, E. W. Sellke, and J. M. DiMaio, "Imaging techniques for clinical burn assessment with a focus on multispectral imaging," Adv. wound care **5**(8), 360–378 (2016).

10. A. Holland, H. Martin, and D. Cass, "Laser doppler imaging prediction of burn wound outcome in children," Burns **28**(1), 11–17 (2002).

11. S. Monstrey, H. Hoeksema, J. Verbelen, A. Pirayesh, and P. Blondeel, "Assessment of burn depth and burn wound healing potential," Burns **34**(6), 761–769 (2008).

12. H. Hoeksema, K. Van de Sijpe, T. Tondu, M. Hamdi, K. Van Landuyt, P. Blondeel, and S. Monstrey, "Accuracy of early burn depth assessment by laser doppler imaging on different days post burn," Burns **35**(1), 36–45 (2009).

13. T. Ida, Y. Kawaguchi, S. Kawauchi, K. Iwaya, H. Tsuda, D. Saitoh, S. Sato, and T. Iwai, "Real-time photoacoustic imaging system for burn diagnosis," J. Biomed. Opt. **19**(8), 086013 (2014).

14. Z. Wu, F. Duan, J. Zhang, S. Li, H. Ma, and L. Nie, "In vivo dual-scale photoacoustic surveillance and assessment of burn healing," Biomedical Optics Express **10**(7), 3425–3433 (2019).

15. S. M. Srinivas, J. F. de Boer, B. H. Park, K. Keikhanzadeh, H.-E. L. Huang, J. Zhang, W. G. Jung, Z. Chen, and J. S. Nelson, "Determination of burn depth by polarization-sensitive optical coherence tomography," J. Biomed. Opt. **9**(1), 207–212 (2004).

16. J. Hardwicke, R. Thomson, A. Bamford, and N. Moiemen, "A pilot evaluation study of high resolution digital thermal imaging in the assessment of burn depth," Burns **39**(1), 76–81 (2013).

17. D. M. Burmeister, A. Ponticorvo, B. Yang, S. C. Becerra, B. Choi, A. J. Durkin, and R. J. Christy, "Utility of spatial frequency domain imaging (SFDI) and laser speckle imaging (LSI) to non-invasively diagnose burn depth in a porcine model," Burns **41**(6), 1242–1252 (2015).

18. A. Ponticorvo, R. Rowland, M. Baldado, G. T. Kennedy, A.-M. Hosking, D. M. Burmeister, R. J. Christy, N. P. Bernal, and A. J. Durkin, "Spatial frequency domain imaging (SFDI) of clinical burns: A case report," Burns Open **4**(2), 67–71 (2020).

19. D. R. King, W. Li, J. J. Squiers, R. Mohan, E. Sellke, W. Mo, X. Zhang, W. Fan, J. M. DiMaio, and J. E. Thatcher, "Surgical wound debridement sequentially characterized in a porcine burn model with multispectral imaging," Burns **41**(7), 1478–1487 (2015).

20. M. H. Arbab, T. C. Dickey, D. P. Winebrenner, A. Chen, M. B. Klein, and P. D. Mourad, "Terahertz reflectometry of burn wounds in a rat model," Biomed. Opt. Express **2**(8), 2339–2347 (2011).

21. L. Rittié, "Cellular mechanisms of skin repair in humans and other mammals," J. Cell Commun. Signal. **10**(2), 103–120 (2016).

22. D. M. Mittleman, R. H. Jacobsen, and M. C. Nuss, "T-ray imaging," IEEE J. Sel. Top. Quantum Electron. **2**(3), 679–692 (1996).

23. Z. Taylor, R. Singh, M. Culjat, J. Suen, W. Grundfest, H. Lee, and E. Brown, "Reflective terahertz imaging of porcine skin burns," Opt. Lett. **33**(11), 1258–1260 (2008).

24. P. Tewari, N. Bajwa, R. S. Singh, M. O. Culjat, W. S. Grundgest, Z. D. Taylor, C. P. Kealey, D. B. Bennett, K. S. Barnett, and A. Stojadinovic, "In vivo terahertz imaging of rat skin burns," J. Biomed. Opt. **17**(4), 040503 (2012).

25. N. Bajwa, S. Sung, D. B. Ennis, M. C. Fishbein, B. N. Nowroozi, D. Ruan, A. Maccabi, J. Alger, M. A. S. John, W. S. Grundfest, and Z. D. Taylor, "Terahertz imaging of cutaneous edema: correlation with magnetic resonance imaging in burn wounds," IEEE Trans. Biomed. Eng. **64**(11), 2682–2694 (2017).

26. P. Tewari, J. Garritano, N. Bajwa, S. Sung, H. Huang, D. Wang, W. Grundfest, D. B. Ennis, D. Ruan, E. Brown, E. Dutson, M. C. Fishbein, and Z. Taylor, "Methods for registering and calibrating in vivo terahertz images of cutaneous burn wounds," Biomed. Opt. Express **10**(1), 322–337 (2019).

27. J. Y. Suen and W. J. Padilla, "Superiority of terahertz over infrared transmission through bandages and burn wound ointments," Appl. Phys. Lett. **108**(23), 233701 (2016).

28. Q. Cassar, S. Caravera, G. MacGrogan, T. Bücher, P. Hillger, U. Pfeiffer, T. Zimmer, J.-P. Guillet, and P. Mounaix, "Terahertz refractive index-based morphological dilation for breast carcinoma delineation," Sci. Rep. **11**(1), 6457 (2021).

29. S. Sung, S. Selvin, N. Bajwa, S. Chantra, B. Nowroozi, J. Garritano, J. Goell, A. D. Li, S. X. Deng, E. R. Brown, W. S. Grundfest, and Z. D. Taylor, "Thz imaging system for in vivo human cornea," IEEE Trans. THz Sci. Technol. **8**(1), 27–37 (2018).

30. S. Sung, S. Dabironezare, N. Llombart, S. Selvin, N. Bajwa, S. Chantra, B. Nowroozi, J. Garritano, J. Goell, A. Li, S. X. Deng, E. Brown, W. S. Grundfest, and Z. D. Taylor, "Optical system design for noncontact, normal incidence, THz imaging of in vivo human cornea," IEEE Trans. THz Sci. Technol. **8**(1), 1–12 (2018).

31. A. Chen, O. B. Osman, Z. B. Harris, A. Abazri, R. Honkanen, and M. H. Arbab, "Investigation of water diffusion dynamics in corneal phantoms using terahertz time-domain spectroscopy," Biomed. Opt. Express **11**(3), 1284–1297 (2020).

32. Y. Deng, J. A. McKinney, D. K. George, K. A. Niessen, A. Sharma, and A. G. Markelz, "Near-field stationary sample terahertz spectroscopic polarimetry for biomolecular structural dynamics determination," ACS Photonics **8**(2), 658–668 (2021).

33. D. I. Ramos-Soto, A. K. Singh, E. Saucedo-Casas, E. Castro-Camus, and M. Alfaro-Gomez, "Visualization of moisturizer effects in stratum corneum in vitro using THz spectroscopic imaging," Appl. Opt. **58**(24), 6581–6585 (2019).

34. H. Lindley-Hatcher, J. Wang, A. I. Hernandez-Serrano, J. Hardwicke, G. Nurumbetov, D. M. Haddleton, and E. Pickwell-MacPherson, "Monitoring the effect of transdermal drug delivery patches on the skin using terahertz sensing," Pharmaceutics **13**(12), 2052 (2021).

35. H. Lindley-Hatcher, A. Hernandez-Serrano, Q. Sun, J. Wang, J. Cebrian, L. Blasco, and E. Pickwell-MacPherson, "A robust protocol for in vivo THz skin measurements," J. Infrared Milli Terahz Waves **40**(9), 980–989 (2019).

36. H. Lindley-Hatcher, A. Hernandez-Serrano, J. Wang, J. Cebrian, J. Hardwicke, and E. Pickwell-MacPherson, "Evaluation of in vivo THz sensing for assessing human skin hydration," JPhys Photonics **3**(1), 014001 (2021).

37. X. Chen, Q. Sun, J. Wang, H. Lindley-Hatcher, and E. Pickwell-MacPherson, "Exploiting complementary terahertz ellipsometry configurations to probe the hydration and cellular structure of skin in vivo," Adv. Photonics Res. **2**, 2000024 (2021).

38. A. Fitzgerald, X. Tie, M. Hackmann, B. Cense, A. Gibson, and V. Wallace, "Co-registered combined OCT and THz imaging to extract depth and refractive index of a tissue-equivalent test object," Biomed. Opt. Express **11**(3), 1417–1431 (2020).

39. H. Cheon, J. H. Paik, M. Choi, H.-J. Yang, and J.-H. Son, "Detection and manipulation of methylation in blood cancer DNA using terahertz radiation," Sci. Rep. **9**(1), 6413 (2019).

40. J.-H. Son, S. J. Oh, and H. Cheon, "Potential clinical applications of terahertz radiation," J. Appl. Phys. **125**(19), 190901 (2019).

41. W. Liu, R. Zhang, Y. Ling, H. Tang, R. She, G. Wei, X. Gong, and Y. Lu, "Automatic recognition of breast invasive ductal carcinoma based on terahertz spectroscopy with wavelet packet transform and machine learning," Biomed. Opt. Express **11**(2), 971–981 (2020).

42. T. Chavez, N. Vohra, K. Bailey, M. El-Shenawee, and J. Wu, "Supervised bayesian learning for breast cancer detection in terahertz imaging," Biomedical Signal Processing and Control **70**, 102949 (2021).

43. B. C. Truong, H. D. Tuan, V. P. Wallace, A. J. Fitzgerald, and H. T. Nguyen, "The potential of the double Debye parameters to discriminate between basal cell carcinoma and normal skin," IEEE Trans. THz Sci. Technol. **5**(6), 990–998 (2015).

44. J. Shi, Y. Wang, T. Chen, D. Xu, H. Zhao, L. Chen, C. Yan, L. Tang, Y. He, H. Feng, and J. Yao, "Automatic evaluation of traumatic brain injury based on terahertz imaging with machine learning," Opt. Express **26**(5), 6371–6381 (2018).

45. N. Qi, Z. Zhang, Y. Xiang, Y. Yang, X. Liang, and P. d. B. Harrington, "Terahertz time-domain spectroscopy combined with support vector machines and partial least squares-discriminant analysis applied for the diagnosis of cervical carcinoma," Anal. Methods **7**(6), 2333–2338 (2015).

46. H. Park and J.-H. Son, "Machine learning techniques for THz imaging and time-domain spectroscopy," Sensors **21**(4), 1186 (2021).

47. M. H. Arbab, D. P. Winebrenner, T. C. Dickey, M. B. Klein, A. Chen, and P. D. Mourad, "A noninvasive terahertz assessment of 2nd and 3rd degree burn wounds," in *CLEO: Science and Innovations*, (Optical Society of America, 2012), pp. CTu3B–3.

48. M. H. Arbab, D. P. Winebrenner, T. C. Dickey, A. Chen, M. B. Klein, and P. D. Mourad, "Terahertz spectroscopy for the assessment of burn injuries in vivo," J. Biomed. Opt. **18**(7), 077004 (2013).

49. O. B. Osman, T. J. Tan, S. Henry, A. Warsen, N. Farr, A. M. McClintic, Y.-N. Wang, S. Arbabi, and M. H. Arbab, "Differentiation of burn wounds in an in vivo porcine model using terahertz spectroscopy," Biomed. Opt. Express **11**(11), 6528–6535 (2020).

50. I. Echchgadda, J. A. Grundt, M. Tarango, B. L. Ibey, T. D. Tongue, M. Liang, H. Xin, and G. J. Wilmink, "Using a portable terahertz spectrometer to measure the optical properties of in vivo human skin," J. Biomed. Opt. **18**(12), 120503 (2013).

51. M. R. Grootendorst, A. J. Fitzgerald, S. G. B. de Koning, A. Santaolalla, A. Portieri, M. V. Hemelrijck, M. R. Young, J. Owen, M. Cariati, M. Pepper, V. P. Wallace, S. E. Pinder, and A. Purushotham, "Use of a handheld terahertz pulsed imaging device to differentiate benign and malignant breast tissue," Biomed. Opt. Express **8**(6), 2932–2945 (2017).

52. Z. B. Harris, M. E. Khani, and M. H. Arbab, "Terahertz portable handheld spectral reflection (phasr) scanner," IEEE Access **8**, 228024–228031 (2020).

53. O. B. Osman, Z. B. Harris, J. W. Zhou, M. E. Khani, A. J. Singer, and M. H. Arbab, "In vivo assessment and monitoring of burn wounds using a handheld terahertz hyperspectral scanner," Adv. Photonics Res. **3**, 2100095 (2022).

54. A. J. Singer, J. W. Zhou, O. B. Osman, Z. B. Harris, M. E. Khani, E. Baer, N. Zhang, S. A. McClain, and M. H. Arbab, "Comparison of comparable scald and contact burns in a porcine model: a preliminary report," Wound Rep. Reg. **28**, 789–796 (2020).

55. T. Brans, R. Dutrieux, M. Hoekstra, R. Kreis, and J. Du Pont, "Histopathological evaluation of scalds and contact burns in the pig model," Burns **20**, S48–S51 (1994).

56. T. Yasui, E. Saneyoshi, and T. Araki, "Asynchronous optical sampling terahertz time-domain spectroscopy for ultrahigh spectral resolution and rapid data acquisition," Appl. Phys. Lett. **87**(6), 061101 (2005).

57. R. J. Dietz, N. Vieweg, T. Puppe, A. Zach, B. Globisch, T. Göbel, P. Leisching, and M. Schell, "All fiber-coupled THz-TDS system with KHz measurement rate based on electronically controlled optical sampling," Opt. Lett. **39**(22), 6482–6485 (2014).

58. Z. B. Harris, O. B. Osman, and M. H. Arbab, "Polarization-sensitive fast THz-TDS scanner in a portable form-factor," in *2020 45th International Conference on Infrared, Millimeter, and Terahertz Waves (IRMMW-THz)* (IEEE, 2020), pp. 01–02.

59. A. Abdullahi, S. Amini-Nik, and M. Jeschke, "Animal models in burn research," Cell. Mol. Life Sci. **71**(17), 3241–3255 (2014).

60. C. J. Andrews, M. Kempf, R. Kimble, and L. Cuttle, "Development of a consistent and reproducible porcine scald burn model," PLoS One **11**(9), e0162888 (2016).
61. B. I. Gómez, M. K. McIntyre, J. M. Gurney, K. K. Chung, L. C. Cancio, M. A. Dubick, and D. M. Burmeister, "Enteral resuscitation with oral rehydration solution to reduce acute kidney injury in burn victims: evidence from a porcine model," PLoS One **13**(5), e0195615 (2018).
62. A. J. Singer, D. Hirth, S. A. McClain, L. Crawford, F. Lin, and R. A. Clark, "Validation of a vertical progression porcine burn model," J. Burn Care & Research **32**(6), 638–646 (2011).
63. J. Kim, D. Dunham, D. Supp, C. Sen, and H. Powell, "Novel burn device for rapid, reproducible burn wound generation," Burns **42**(2), 384–391 (2016).
64. A. Ponticorvo, D. M. Burmeister, B. Yang, B. Choi, R. J. Christy, and A. J. Durkin, "Quantitative assessment of graded burn wounds in a porcine model using spatial frequency domain imaging (SFDI) and laser speckle imaging (LSI)," Biomed. Opt. Express **5**(10), 3467–3481 (2014).
65. C. J. Andrews and L. Cuttle, "Comparing the reported burn conditions for different severity burns in porcine models: a systematic review," Int. Wound J. **14**, 1199–1212 (2017).
66. A. J. Singer, L. Berruti, H. C. Thode Jr, and S. A. McClain, "Standardized burn model using a multiparametric histologic analysis of burn depth," Academic Emergency Med. **7**, 1–6 (2000).
67. Z. B. Harris, A. Virk, and M. H. Arbab, "Handheld telecentric THz-TDS scanner using custom f-θ optics for imaging applications in clinical settings and non-destructive testing," in 2019 44th International Conference on Infrared, Millimeter, and Terahertz Waves (IRMMW-THz) (IEEE, 2019), p. 1.
68. Z. B. Harris, A. Virk, M. E. Khani, and M. H. Arbab, "Terahertz time-domain spectral imaging using telecentric beam steering and an f-θ scanning lens: distortion compensation and determination of resolution limits," Opt. Express **28**(18), 26612–26622 (2020).
69. Z. B. Harris, S. Katletz, M. E. Khani, A. Virk, and M. H. Arbab, "Design and characterization of telecentric f-θ scanning lenses for broadband terahertz frequency systems," AIP Adv. **10**(12), 125313 (2020).
70. Y. Kim and D.-S. Yee, "High-speed terahertz time-domain spectroscopy based on electronically controlled optical sampling," Opt. Lett. **35**(22), 3715–3717 (2010).
71. M. E. Khani, D. P. Winebrenner, and M. H. Arbab, "Phase function effects on identification of terahertz spectral signatures using the discrete wavelet transform," IEEE Trans. THz Sci. Technol. **10**(6), 656–666 (2020).
72. M. E. Khani and M. H. Arbab, "Chemical identification in the specular and off-specular rough-surface scattered terahertz spectra using wavelet shrinkage," IEEE Access **9**, 29746–29754 (2021).
73. Y. Chen, S. Huang, and E. Pickwell-MacPherson, "Frequency-wavelet domain deconvolution for terahertz reflection imaging and spectroscopy," Opt. Express **18**(2), 1177–1190 (2010).
74. M. H. Arbab, A. Chen, E. I. Thorsos, D. P. Winebrenner, and L. M. Zurk, "Effect of surface scattering on terahertz time domain spectroscopy of chemicals," Proc. SPIE **6893**, 68930C (2008).
75. X. Glorot and Y. Bengio, "Understanding the difficulty of training deep feedforward neural networks," in *Proceedings of the Thirteenth International Conference on Artificial Intelligence and Statistics* (JMLR Workshop and Conference Proceedings, 2010), pp. 249–256.
76. O. B. Osman and M. H. Arbab, "Mitigating the effects of granular scattering using cepstrum analysis in terahertz time-domain spectral imaging," PLoS One **14**(5), e0216952 (2019).
77. M. E. Khani, O. B. Osman, and M. H. Arbab, "Diffuse terahertz spectroscopy in turbid media using a wavelet-based bimodality spectral analysis," Sci. Rep. **11**(1), 1–13 (2021).
78. M. H. Arbab, D. P. Winebrenner, E. I. Thorsos, and A. Chen, "Application of wavelet transforms in terahertz spectroscopy of rough surface targets," in *Terahertz Technology and Applications III*, vol. 7601 L. P. Sadwick and C. M. M. O'Sullivan, eds. (SPIE, 2010), pp. 43–49.
79. J. Wang, H. Lindley-Hatcher, X. Chen, and E. Pickwell-MacPherson, "THz sensing of human skin: a review of skin modeling approaches," Sensors **21**(11), 3624 (2021).
80. J. Seok, H. S. Warren, A. G. Cuenca, M. N. Mindrinos, H. V. Baker, W. Xu, D. R. Richards, G. P. McDonald-Smith, H. Gao, L. Hennessy, C. C. Finnerty, C. M. López, S. Honari, E. E. Moore, J. P. Minei, J. Cuschieri, P. E. Bankey, J. L. Johnson, J. Sperry, A. B. Nathens, T. R. Billiar, M. A. West, M. G. Jeschke, M. B. Klein, R. L. Gamelli, N. S. Gibran, B. H. Brownstein, C. Miller-Graziano, S. E. Calvano, P. H. Mason, J. P. Cobb, L. G. Rahme, S. F. Lowry, R. V. Maier, L. L. Moldawer, D. N. Herndon, R. W. Davis, W. Xiao, and R. G. Tompkins, the Inflammation, and Host Response to Injury, Large Scale Collaborative Research Program, "Genomic responses in mouse models poorly mimic human inflammatory diseases," Proc. Natl. Acad. Sci. **110**(9), 3507–3512 (2013).
81. M. H. Arbab, P. D. Mourad, A. Chen, T. C. Dickey, M. D. Klein, and D. P. Winebrenner, "Methods and systems for assessing a burn injury," US Patent No. US9295402B1 (2016).